Interactive Visualization of Scattered Moment Tensor Data

Harald Obermaier[a,c], Magali I. Billen[b], Hans Hagen[a] and Martin Hering-Bertram[c]

[a]University of Kaiserslautern, Germany
[b]University of California Davis, USA
[c]Fraunhofer ITWM, Kaiserslautern, Germany

ABSTRACT

Moment tensors derived from seismic measurements during earthquakes are related to stress tensors and keep important information about surface displacement in the earth's mantle. We present methods facilitating an interactive visualization of scattered moment data to support earthquake and displacement analysis. For this goal, we combine and link visualizations of spatial location and orientation information derived from moment tensor decompositions. Furthermore, we contribute new tensor glyphs highlighting the indefinite character of moment tensors as well as novel tensor clustering and averaging techniques to aid interactive visual analysis and ease the challenges of interpreting moment tensor data.

Keywords: moment tensor, tensor glyph, clustering, interactive

1. INTRODUCTION

Tensors from applications such as Diffusion Tensor Magnetic Resonance Imaging (DT-MRI)[1] have gained widespread attention over the last years, leading to the development of sophisticated extraction and rendering techniques for medical data visualization. A different source of tensors that is comparatively less known to the visualization community are seismic earthquake measurements in geoscience. Hereby, seismic sensors at locations close to points of interest such as known or suspected faults generate a scattered set of symmetric second order moment tensors describing earthquake point sources leading to displacement of the earth's surface.

This scattered tensor field carries valuable information about earthquake magnitude, type, wave polarity and fault orientation. We present novel tensor glyphs to visualize these properties for individual moment tensors. Interpolation in moment tensor fields is a challenging task, as different source types, such as artificial explosions and natural shear dislocation have to be treated separately. To overcome this problem, we introduce novel tensor clustering and averaging methods as well as accompanying visualization techniques. Tensors of resulting clusters can be combined and averaged into one representative glyph, which additionally contributes to glyph-based field visualization by reducing visual occlusion and clutter. The spatial nature of the information conveyed by placing tensor glyphs at positions of measurements is complemented by a visualization of the overall orientation data present in the data in the form of a hemisphere stereographic projection. This allows us to depict clustering and orientation not only in three dimensions but also in the projective space of orientations. Furthermore, we provide interaction methods to intuitively match data between both spaces. While the presented methods may be used for the illustration of stress tensors in general, they have been applied to different real world moment tensor data sets to produce the results presented in this paper. Main contributions to the visualization community are:

- Novel moment tensor clustering and averaging technique.
- Glyph based visualization of indefinite moment tensors by polarity glyphs and slip geometry.
- Linked spherical-projective and spatial visualization techniques for moment tensor visualization.

Section 2 provides an overview of existing work in the field of moment tensors and tensor visualization. In section 3, we give an introduction to properties, types and sources of moment tensors. Section 4 proposes new glyph techniques to highlight important characteristics of moment tensors before introducing tensor clustering and averaging in section 5. We build upon these findings, to describe properties and interaction techniques of the two spaces used for visualization of scattered moment data in section 6. Results are given in section 7, whereas section 8 concludes this paper.
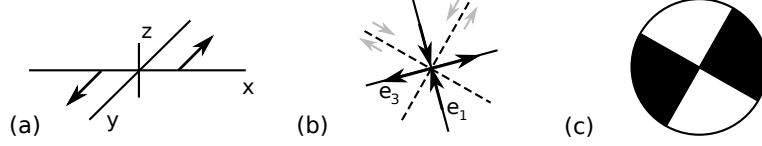
Figure 1. (a) Vector couple corresponding to m_{yx}. (b) Force dipoles in rotated system corresponding to pure shear. Stippled lines represent the two possible fault plan orientations. (c) Beachball representation of the situation in (b).

2. RELATED WORK

Most tensor field visualization techniques[2] focus on either local properties of individual tensors or global behavior of the tensor field while neglecting similarity on a tensor basis. Visualization of local attributes of the tensors is commonly achieved by utilizing shapes, icons or glyphs to depict relevant tensor properties, as done by superquadric glyphs,[3] Reynolds glyphs[4] or others, whereas methods that need a global topology-based analysis of the field make use of stream line extraction along tensor eigenvectors.[5] To depict moment tensors, Ohtsu et al.[6] use VRML and simple plane glyphs that are limited to the depiction of fault planes and movement. Another publication in the area of moment tensor visualization[7] uses dense visualization of shapes on a regular grid to depict eigenvector directions and magnitude. However, the used data is neither scattered, nor do they perform clustering. In general, when tensor fields are sampled in a significantly dense manner or allow straight-forward interpolation of tensors, a global view of the data can be achieved by dense or intelligent glyph placing.[8] In contrast to these methods, we aim to give a global view of tensor properties in a scattered data set, while avoiding the drawback of classic tensor interpolation. In the context of clustering, Rohlfing et al.[9] make use of k-means diffusion-tensor clustering based on probability distributions for averaging and interpolation between DT-MRI scans. Regarding moment tensors, similarity measures based on the inner matrix product[10] have been used for simple cluster identification, a definition that we extend in this work. So far, the tensor visualization community has mainly focused on diffusion tensors. We introduce methods that are not specific to diffusion tensors, but aim to improve moment tensor analysis and are applicable to a variety of symmetric second order tensor fields.

3. MOMENT TENSOR

Seismic sensors recording waves emitted during earthquakes, indicating surface displacement along faults. A well-established way of capturing these displacement discontinuities of the earth's surface is their representation as force couples in moment tensors.[11] The seismic moment tensor M is a symmetric 3×3 tensor. Components m_{ij} denote the magnitude of the moment caused by the force couple in i-direction acting on the j-direction. Figure 1 (a) illustrates one of nine possible force couples. The vanishing angular moment in the seismic source implies symmetry, i.e. $m_{ij} = m_{ji}$. In the following we present fundamental properties of such tensors.

3.1 Fault Representation

An important information represented by moment tensors is the orientation of displacement discontinuities or fault planes in the earth's mantle. Due to symmetry, a moment tensor M can be diagonalized by rotation into its eigenvector system, with entries on the diagonal corresponding to its eigenvalues. For pure slip along a plane, M has eigenvalues $\lambda_1 < \lambda_2 < \lambda_3$ with $\lambda_1 = -\lambda_3$ and $\lambda_2 = 0$, see (1). Such moment tensors are therefore known to be *pure double-couple* (DC) tensors.

$$M^{DC} = \begin{pmatrix} \lambda_1 & 0 & 0 \\ 0 & \lambda_2 & 0 \\ 0 & 0 & \lambda_3 \end{pmatrix} = \begin{pmatrix} -\lambda_3 & 0 & 0 \\ 0 & 0 & 0 \\ 0 & 0 & \lambda_3 \end{pmatrix} \tag{1}$$

In the rotated coordinate system where $-\lambda_3 = m_{11}^{DC}$ and $\lambda_3 = m_{33}^{DC}$, the corresponding eigenvector directions e_1 and e_3 represent two orthogonal force dipole directions of opposing forces, as shown in Figure 1 (b). Due to displacement magnitude and direction, possible fault plane directions are rotated by 45° with respect to the principal axis directions. Only analysis of further seismic activities can help select the true fault plane direction from these two orthogonal candidate planes.

3.2 Tensor Decomposition and Properties

Due to measurement errors, complex faulting behavior, and other sources, eigenvalues of real-world moment tensors do not always have the properties described in 3.1 and do not generally represent pure double-couple tensors. A tensor decomposition proposed in[12] allows measurement of the contribution of a pure double-couple and other sources. According to this decomposition, a diagonalized tensor M consists of the following components:

$$M = M_{iso} + M_{dev} = M_{iso} + aM_{dc} + bM_{clvd} = M_{iso} + a \begin{pmatrix} -1 & 0 & 0 \\ 0 & 0 & 0 \\ 0 & 0 & 1 \end{pmatrix} + b \begin{pmatrix} -1 & 0 & 0 \\ 0 & -1 & 0 \\ 0 & 0 & 2 \end{pmatrix} \tag{2}$$

where M_{iso} is the isotropic part of the tensor and M_{dev} the deviatoric part, which is decomposed into a double-couple component M_{dc} and a *compensated linear vector dipole* (CLVD) component M_{clvd}, with a and b depending on the eigenvalues of M. While this is not the only valid moment tensor decomposition, it allows classification of moment tensors into seismic events with mainly isotropic parts (explosions or implosions), mainly DC parts (slip along a single fault), and large CLVD components (slips along multiple faults, planar movement, or volcanic activities). As presented in a later section, this allows predictions about moment tensor glyph shapes. During data analysis or processing, moment tensors are often represented by an approximating best double-couple, neglecting isotropic or CLVD contributions.

In contrast to tensor data caused by man-made explosions, moment tensors derived from wave emissions of natural causes are usually traceless tensors, because these movements cause no changes in volume. Therefore, positive wave polarity along one direction is always accompanied by negative displacement along another direction, as indicated by opposing signs in the tensor eigenvalues. Thus, such moment tensors are indefinite and

$$\exists_{v,w} : \ v^T \cdot M \cdot v > 0 \ \wedge \ w^T \cdot M \cdot w < 0 \tag{3}$$

with $v, w \in \mathbb{R}^3$ holds. This important property of the quadratic form $q_M(v) = v^T \cdot M \cdot v$ can be used directly for tensor visualization, as detailed in the next section. Two additional quantities representing the seismic moment M_0 and the resulting moment magnitude M_w may be derived from moment tensor data:

$$M_0 = \sqrt{\frac{1}{2} \sum_{ij} m_{ij}^2} \qquad M_w = \frac{2}{3} log_{10} M_0 - 10.7 \tag{4}$$

These scalars provide means to measure the size of an earthquake.

4. MOMENT TENSOR GLYPHS

As described earlier, tensor glyphs are the preferred way to visualize tensor properties. Beachball glyphs as shown in Figure 1 (c) for a pure double-couple are the classic way to depict fault plane orientations of moment tensors, where a circle is shaded according to wave polarity. Black indicates tensional, white compressional forces. Fault plane candidates can be perceived from the glyphs, as they are aligned with the borders between black/white quadrants. Positive (negative) definite tensors yield completely black (white) glyphs, while CLVD moment tensors lead to non-orthogonal shading of the glyphs. Most publications focus on the depiction of the double-couple component of a moment tensor to identify prevailing fault plane orientations. However, neither do these glyphs convey clear information about relative amplitudes of waves even when the shapes are scaled by M_0 or M_w to show earthquake magnitude, nor do they always provide a clear look at slip directions. We overcome these drawbacks by exploiting the fact that most moment tensors are indefinite and carry important information in their quadratic form.
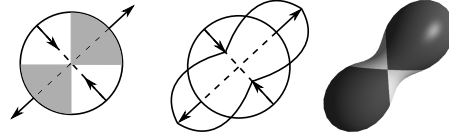
Figure 2. Standard beachball and glyph shape offsets according to q_M. The shape of the resulting glyph conveys direction and magnitude information.
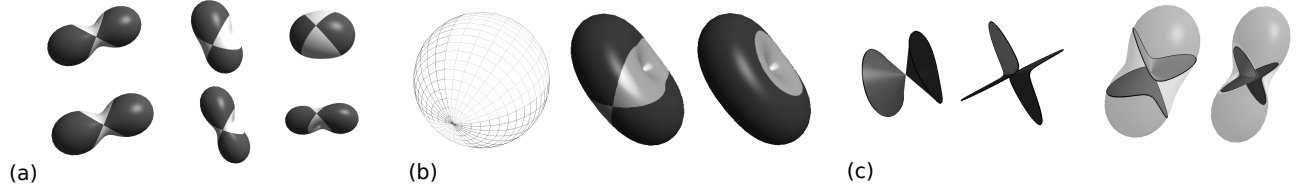

(a) (b) (c)

Figure 3. Gray-scale images of: (a) Glyphs scaled according to method one (top) and two (bottom). Texture shows orientation of the best double-couple. (b) Rotated mesh and glyph with large CLVD component, showing DC and polarity shading. (c) Slip geometry glyphs for high CLVD and high DC tensors can be combined with polarity glyphs.

4.1 Polarity Glyphs

For positive definite diffusion tensors, several authors[1] have proposed to visualize M by rendering the implicit glyph $q_M(v) = c$ or $q_{M^{-1}}(v) = c$ for a constant $c \in \mathbb{R}^+$, thus depicting scaling and diffusion properties of the tensor. In contrast to these methods, we use the quadratic form q_M to modulate a basic glyph shape to visualize wave polarity and amplitude of indefinite tensors. The final glyph shape is desired to allow distinction between sources with different wave polarities, directions, absolute and relative amplitudes. Given an arbitrary unit vector in spherical coordinates $v(\theta, \phi) \in \mathbb{R}^3$, $q_M(v)$ represents the signed magnitude of the force couple in direction of v. For $v = e_i$, $i \in \{1, 2, 3\}$, the quadratic form evaluates to the corresponding eigenvalue. Motivated by these properties, vertices of an isotropic mesh can be modified to produce the desired glyphs, as seen in Figure 2:

1. Create a spherical mesh S with radius r
2. Compute $q_M(v/||v||)$ for every vertex $v \in S$
3. Displace mesh points v by $d_M(v) = c \cdot q_M(v/||v||) \cdot \frac{v}{||v||}$

Both r and c are determined by the desired scaling preferences described in the following. For a given set of moment tensors, seismic moments and therefore extremal values of q_M may vary strongly. The straightforward approach to yield consistent glyph scaling over a set of moment tensors is to choose $c = \frac{r}{max_M(|q_M|)}$ and fix r to a constant value over the data set. This way relative differences in glyph shape displacements d_M are equivalent to relative differences in seismic moments. Furthermore, glyphs shapes do not self intersect, as $||d_M(v)|| \leq r$ holds for all M. While this method accurately and consistently reflects force magnitudes by glyph displacements, glyphs with comparatively small wave amplitudes degenerate to sphere-like shapes as observable in Figure 3 (a), as earthquake magnitudes are reflected in glyph silhouettes directly. As a second method, we choose $c = \frac{r}{max_v(|q_M|)}$ with r proportional to M_w for every glyph individually. This results in glyphs that show accurate force and displacement ratios within a glyph and represent differences in earthquake magnitude between glyphs by uniform scaling. The advantage of latter method is the clearer depiction of directions and polarity of maximal forces. A drawback of this uniform scaling in three dimensions is, however the ambiguity of size and distance, which requires earthquake magnitude to be mapped to an additional visual parameter such as color.

4.1.1 Visualization

Following the shading convention of beachball glyphs, we make use of texturing to either highlight the best double-couple of a glyph by appropriate shading of the quadrants, or map positive and negative polarity to different colors. Figure 3 (b) shows examples of both shading types. Polarity based shading allows easy identification of

tensors with large isotropic or CLVD components. We note that spherical meshes are rotated prior to vertex displacement, to ensure that high resolution poles of the discretized mesh coincide with the direction of e_2. This allows accurate texturing of the region where the four quadrants meet. All glyphs are shaded and textured using pixel shaders to avoid visual artifacts resulting from low resolution meshes and aid in conveying glyph shape properties such as curvature. In comparison to beachball renderings, polarity glyphs are able to not only represent fault plane orientation but CLVD and isotropy fractions and absolute displacement magnitudes as well.

4.2 Slip Geometry

As noted by Haller[13, 14] in the context of flow vortices, indefinite matrices describe a partition of local space into sections with attracting and repelling flow behavior. The polarity glyphs introduced in the last section encode this attracting and repelling behavior in the context of wave propagation and force orientation by shading surface areas accordingly. To convey the full shape of this flow separation or fault geometry, we propose a method to extract slip geometry G_S of a tensor directly. For a given indefinite tensor, the quadratic form q_M defines a unique scalar field on the unit-sphere, with a zero set $\{v|q_M(v) = 0\}$ corresponding to the closed boundary between regions of inflow and outflow or opposing force directions. In moment tensor data, this boundary indicates slip geometry. To extract this geometry, we discretize the unit-sphere uniformly along its spherical coordinates θ and ϕ. The resulting grid cells $[i\Delta\theta, (i + 1)\Delta\theta] \times [j\Delta\phi, (j + 1)\Delta\phi]$ are quads in spherical coordinate space and thus qualify for standard isocontour extraction techniques. For the isovalue of $q_M(v) = 0$, performing the standard Marching Quads algorithm on these cells yields a connected set of lines on the unit-sphere. Slip geometry triangles are created by connecting these line segments with the origin of the unit sphere. These triangles are a valid representation of G_S, as $q_M(w) = 0$ holds for all w with $v^T \cdot \frac{w}{||w||} = 1$.

As isotropic tensors do not contain a distinct direction of slip, we only apply this method to anisotropic tensors, as common in real world data sets.

4.2.1 Visualization

Visualizations of G_S for different moment tensors are shown in Figure 3 (c). Highlighted rendering of glyph boundaries helps distinguish different slip geometry types. Slip and polarity glyph types complement each other when combined. Pure double-couple tensors produce two perpendicular flat sphere segments as expected, whereas CLVD tensors produce more complex geometries due to different contributions of a number of double-couple fault planes to the final shape of the glyph. In contrast to beachball or polarity glyphs, this extracted geometry gives a clear look at interior displacement discontinuities. Highest information density is reached when combined with transparent polarity glyphs.

5. CLUSTERING AND AVERAGING

The presented glyphs facilitate a local visualization and analysis of scattered moment tensor fields. As straightforward interpolation of scattered moment tensors is not feasible due to the loss of important tensor properties when mixing different source types, tensor grouping or averaging has to rely on additional clustering steps. For an insightful visualization of the complete tensor field, several reasons motivate the averaging and clustering of multiple tensors into subsets. A first reason is given by visual occlusion that frequently appears in regions with a high density of seismic activities being represented by large and dense groups of moment tensor glyphs. A second reason is the fact that accumulations of spatially close moment tensors commonly represent similar faulting mechanisms. Similar faulting mechanisms may be summarized into an abstract average seismic event, thus reducing information overload. Another reason for moment tensor clustering is the identification of locations and properties of frequently active seismic sources. In the following, we present a selection of moment tensor similarity measures and introduce a novel tensor clustering method along with an averaging procedure, allowing efficient computation and visualization of tensor clusters.

5.1 Similarity Measures

For diffusion tensors, a number of metrics were proposed over the last decades.[15] Among others, Kagan[16] and Willemann[10] present similarity measures for moment tensors. While Kagan defines similarity between moment tensors as the minimum angle needed to transform one double-couple into another by rotation, Willemann uses
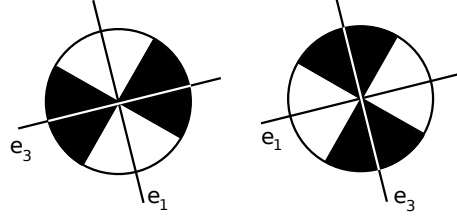
Figure 4. Moment tensors of different earthquakes with identical fault geometry. $\alpha_{min} = \Pi$, $\hat{\alpha}_{min} = 0$, $S = \Pi$ and $\hat{S} = 0$.

the inner tensor product to define similarity on the full tensor rather than the best double-couple. In the following we summarize both approaches and introduce modifications to allow source-type clustering.

5.1.1 Double-Couple Rotation

The double-couple orientation of a moment tensor is fully described by the eigenvector system of the tensor. For a fixed ordering of eigenvectors such as $e_x, e_y, e_z \simeq e_1, e_2, e_3$, this orthogonal system can be converted into a unit-quaternion[17] representation $Q = (cos(\alpha/2), sin(\alpha/2) \cdot q) = (q_0, q_1, q_2, q_3)$ by:

$$\begin{pmatrix} e_1 & e_2 & e_3 \end{pmatrix} = \begin{pmatrix} q_0^2 + q_1^2 - q_2^2 - q_3^2 & 2(q_1 q_2 - q_0 q_3) & 2(q_1 q_3 + q_0 q_2) \\ 2(q_1 q_2 + q_0 q_3) & q_0^2 - q_1^2 + q_2^2 - q_3^2 & 2(q_2 q_3 - q_0 q_1) \\ 2(q_1 q_3 - q_0 q_2) & 2(q_2 q_3 + q_0 q_1) & q_0^2 - q_1^2 - q_2^2 + q_3^2 \end{pmatrix} \tag{5}$$

This right-handed (left-handed) coordinate system is not unique but results in 4 different quaternions depending on choice of eigenvector signs, from which one commonly chooses the solution with minimal rotation angle to the canonical coordinate frame. For quaternions Q_M, Q_N of two moment tensors, the minimal angle of rotation between double-couples of M and N corresponds to

$$\alpha_{min}(M, N) = 2 \cdot cos^{-1}(max_q((Q_M \cdot q \cdot Q_N^{-1})_0)) \tag{6}$$

where $q \in \{(1, 0, 0, 0), (0, 1, 0, 0), (0, 0, 1, 0), (0, 0, 0, 1)\}$, and $(.)_0$ corresponds to the scalar component q_0 of a quaternion. This distance function α_{min} can be used to define a similarity measure on double-couples. Thus, when neglecting CLVD and isotropic components of moment tensors, this defines a metric on the approximating double-couples of arbitrary moment tensors (with the exception of isotropic tensors).

We modify this distance function to not only serve as a similarity measure on seismic wave propagation of earthquakes, but as well on fault geometry, see Figure 4. After computing α_{min}, we repeat computation of α_{min} with swapped directions e_1 and e_3 in the coordinate system of one of the two moment tensors. The overall minimal angle $\hat{\alpha}_{min}$ of both computations is equal to the minimal angle needed to rotate one fault plane system into the other, as illustrated in Figure 4. While slipping directions of moment tensors that are similar to each other with respect to $\hat{\alpha}_{min}$ may have opposing directions, this measure identifies moment tensors based on similarity of fault geometry.

5.1.2 Full Tensor Similarity

In contrast to the double-couple similarity measure described above, this distance function is not restricted to approximating double-couples, but operates on the full moment tensor data. For two second order square tensors M, N with $\sum_i \lambda_i^2 = 2$, the inner tensor product

$$M \cdot N = \sum_{ij} m_{ij} \cdot n_{ij} \tag{7}$$

is a natural measure of tensor similarity. Values of the product are limited to the interval $[-2, 2]$ with $M \cdot M = 2$ and $M \cdot -M = -2$. A function

$$S(M, N) = cos^{-1}\left(\frac{M \cdot N}{2}\right) \tag{8}$$

defines a distance between arbitrary normalized moment tensors M and N. S is maximal for opposing moment tensor pairs, i.e. for moment tensor pairs with identical orientation in the eigenvector system and opposite eigenvalue signs. We again propose a modified similarity measure by identifying moment tensors with identical fault orientations. For this matter, we replace $M \cdot N$ by $|M \cdot N|$ in the computation of S to yield a new distance measure $\hat{S}$ with similar properties as $\hat{\alpha}_{min}$ as indicated in Figure 4. In contrast to $\hat{\alpha}_{min}$, this distance function is able to operate on purely isotropic tensors as well. Aside from this fact, choice of the similarity measure is based on whether to include CLVD components into the clustering algorithm or not. If the data is suspected to contain a lot of noise, causing pure double-couple sources to include incorrect CLVD components, the first measure might therefore be preferred over the latter.

In the following the four presented distance functions will be used to realize interactive and automatic tensor clustering. It is important to note that both presented distance measures ignore the magnitude of the seismic moment either by using the eigenvector system directly, or by operating on normalized tensors.

5.2 Clustering

Clustering serves to group and identify similarities in arbitrary data sets where its data reduction and information densification properties make it a prime candidate to be applied to cluttered tensor glyph visualizations. In the context of this work, tensor clusters have to fulfill two properties. Firstly, tensors in a cluster have to be significantly similar to each other, secondly clusters should be constrained to a local neighborhood to avoid grouping of spatially separate tensors. A clustering of objects based on a similarity measure fulfilling the first property is given by the Quality-Threshold Clustering (QT) algorithm.[18] To satisfy the second property, we propose a Distance-QT Clustering algorithm utilizing a minimum spanning tree representation of each cluster.

5.2.1 Distance-Quality-Threshold Clustering

Our DQT-Clustering algorithm is a modified version of the classic QT-Clustering method that additionally imposes euclidean distance constraints on the final clusters. Input parameters of the clustering algorithm are a distance function d such as α_{min}, a threshold ϵ_d that specifies the maximal allowed distance in similarity between two members of a cluster and a euclidean distance threshold ϵ_e defining the maximal euclidean distance between nearest neighbors of a cluster. The clustering algorithm takes the following form:

1. Let U denote the set of unclustered tensors and C_C the set of clusters.
2. Choose a tensor $M \in U$, starting a new candidate cluster $C_M = \{M\}$.
3. Add $argmin_{P \in U/C_M}(max_{N \in C_M}(d(P, N)))$ to C_M, until $max_{N \in C_M}(d(P, N)) > \epsilon_d$ for all $P \in U/C_M$.
4. Build a euclidean minimum spanning tree for C_M.
5. Remove all parts of C_M that are connected to M by an edge larger than ϵ_e.
6. Repeat from 2 with an unvisited $M \in U$, until all tensors in U have generated a candidate cluster.
7. Add the largest candidate add to C_C. Remove its members from U. Clear all candidate clusters.
8. Repeat from 2, until $U = \emptyset$.

When execution of the algorithm has finished, C_C contains non-overlapping tensor clusters. With exception of steps four and five, this clustering algorithms is identical to the standard QT method. In step three the point P that minimizes the maximal distance to all members of the candidate cluster C_M is added to the set, if $max_{N \in C_M}(d(P, N)) > \epsilon_d$. This guarantees complete linkage clustering, i.e. the maximal distance with respect to d between two arbitrary members of a cluster is limited by ϵ_d. To minimize computational complexity, we pre-compute d for pairs of moment tensors during loading of the data set, thus ensuring reduced computation times during clustering.

While these steps yield clustering in the space of tensor similarity, they do not impose constraints on euclidean space, resulting in clusters that are distributed over large parts of the scattered tensor field. To enforce spatial
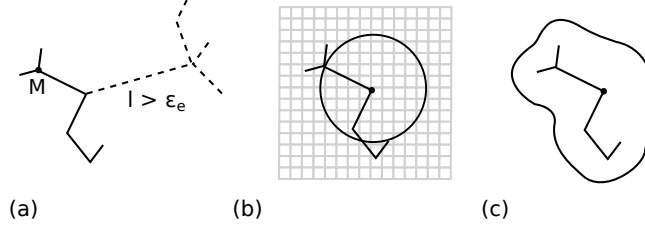
Figure 5. (a) Minimum spanning tree for a set of points in $\mathbb{R}^2$. Parts of the tree are removed, as connecting edges exceed ϵ_e. (b) Metaball radius for a selected node with underlying extended cluster bounding box. (c) Illustration of final cluster outline.

locality of moment tensor clusters, we introduce a cluster splitting method based on minimum spanning trees. For a set of objects in euclidean space, a euclidean minimum spanning tree corresponds to a tree representation of the set with a minimal total of edge lengths among all trees that can be constructed from that set. We construct the minimum spanning tree for a candidate cluster using Prim's algorithm. By removing objects from the cluster that are connected to M by edges exceeding the pre-defined threshold ϵ_e, cluster locality is guaranteed, as illustrated by Figure 5 (a). Connectivity information gathered in this tree-building process is saved for visualization purposes.

5.3 Tensor Averaging

Clusters obtained by the described method facilitate local tensor averaging while excluding tensors of strongly dissimilar types, leading to an accurate representation of a closed set of moment tensors. Given a cluster of moment tensors M_i, we compute a representative tensor M_a by averaging of eigenvector directions and eigenvalues of cluster members. For M_i, $i \in \{1, .., n\}$ with ordered eigenvectors e_1^i, e_2^i, e_3^i, eigenvectors of M_a evaluate to

$$(e_1^a, e_2^a, e_3^a) = \left(\frac{\sum_i e_1^i}{|| \sum_i e_1^i ||}, \frac{\sum_i e_2^i}{|| \sum_i e_2^i ||}, \frac{\sum_i e_3^i}{|| \sum_i e_3^i ||} \right) \tag{9}$$

where eigenvectors e^i are oriented according to a chosen right-hand coordinate system implied by (e_1^0, e_2^0, e_3^0) to avoid ambiguity. Eigenvectors of isotropic sources are omitted; corresponding eigenvalues are averaged similarly. If $\hat{\alpha}_{min}$ or $\hat{S}$ was used during clustering, e_1^i and e_3^i may be swapped during the averaging process to correspond to the directions of e_1^0 and e_3^0. From this eigenvector system, the average pseudo moment tensor is reconstructed by solving

$$M_a \cdot \begin{pmatrix} e_1^a & e_2^a & e_3^a \end{pmatrix} = \begin{pmatrix} \lambda_1^a \cdot e_1^a & \lambda_2^a \cdot e_2^a & \lambda_3^a \cdot e_3^a \end{pmatrix}. \tag{10}$$

Glyphs of these average tensors show an accurate representation of average fault plane directions and polarity magnitudes. For source type clustering we limit display of average tensors to slip geometry glyphs, as wave polarity is neglected during that type of clustering. The representative glyph of a cluster is placed at the position of an edge of the minimum spanning tree that is closest to the centroid of the cluster's bounding box.

5.3.1 Cluster Visualization

While classic ways of visualizing object clusters by distinct object colors or shapes allow visual distinction of clusters, they often fail to convey a homogeneous representation of a cluster and rely on the visual presence of cluster members. Cluster outlining techniques avoid these problems. We propose a cluster outlining technique based on implicit metaball shapes[19, 20] to allow consistent cluster visualization in the absence of cluster members. The minimum spanning tree skeleton obtained during clustering provides connectivity information in a cluster and can be used in the process of visualization. For cluster outline generation we center an energy function

$$f(p_i, p) = max \left(0, \left(1 - \frac{||p - p_i||^2}{r_i^2} \right)^3 \right) \tag{11}$$

at every member tensor position p_i with a radius r_i corresponding to the maximal length of adjacent edges in the minimum spanning tree, as seen in Figure 5 (b). This energy function has similar properties as the commonly used Gaussian function, but has an important advantage in evaluation speed. The accumulation of energy functions in a cluster yields a three-dimensional scalar field, that serves as basis for isovolume extraction. For discretization purposes, the cluster is enclosed by an extended version of its axis aligned bounding box with coordinates $(x_0, y_0, z_0, x_1, y_1, z_1) = (min_i((p_i)_x) - max_i(r_i), min_i((p_i)_y) - max_i(r_i), min_i((p_i)_z) - max_i(r_i), max_i((p_i)_x) + max_i(r_i), max_i((p_i)_y) + max_i(r_i), max_i((p_i)_z) + max_i(r_i)$ and sampled by a uniform grid, see Figure 5 (b). Scalar values $s(.)$ at grid node positions g_j are evaluated as $s(g_j) = \sum_i f(p_i, g_j)$. We use the standard Marching Cubes technique to extract a triangulated isovolume for a value of 0.6 in the resulting uniformly sampled scalar field. Hereby, empirical choice of isovalue and choice of the r_i produce a connected outline of the cluster.

A rendering of this isovolume geometry may be used for direct cluster visualization. However, we restrict rendering of these isovolumes to their view dependent silhouettes to provide a clear look at the cluster contents. To achieve this, we make use of the OpenGL stencil buffer to mask out irrelevant parts of the isovolume:

1. Choose a cluster C with $|C| > 1$.
2. Clear the stencil buffer bits to 1.
3. Draw the triangulated isovolume of C to the stencil buffer only, setting covered bits to 0.
4. Draw an the enlarged isovolume with shading and coloring to pixels where the stencil buffer is 1.
5. Repeat from 1 until all desired clusters are drawn.

An enlarged version of the isovolume used during rendering in step 4 is obtained by displacing isovolume vertices along their normals. As a result of this rendering technique, a view dependent outline of the cluster is drawn, providing a clear view at inner parts of the cluster, while depicting the silhouette of the cluster. An illustration is given in Figure 5 (c). These outlines provide a visual clue about cluster dimensions, even if no cluster members are drawn.

6. INTERACTIVE VISUALIZATION

We have described methods to visualize and cluster scattered moment tensor fields in $\mathbb{R}^3$. This section details how to enhance visualization of such fields by the addition of an interactive projective rendering of the data set.

6.1 Stereonet Display

Lower hemisphere stereographic projections, or *stereonets* are angle preserving projective mappings that are frequently used in geoscience to analyze orientations of moment tensor data. A generalized stereographic projection for a projection point P on the unit-sphere maps points P_i on the unit-sphere surface to the intersection point of the line $g_i(t) = P + t(P - P_i)$ with the plane orthogonal to $(O - P)$ going through the origin. This mapping is undefined for P and is restricted to the hemisphere opposite to P in the following. An illustration of the mapping process along with a concrete example of a projected hemisphere are shown in Figure 6 (a) and (b). To give a global impression of fault directions and moment tensor orientations, we extend the three-dimensional rendering context by a viewport showing such a stereonet type visualization. We render moment tensor orientations as points on the unit-sphere corresponding to minor and major eigenvector directions of the tensors. Major eigenvector directions are traditionally rendered as filled, minor eigenvector directions as empty dots. Due to orthogonality, the double-couple and fault plane directions of a moment tensor are uniquely defined by these two positions. As we detail in the results section, this view allows detailed cluster analysis of moment tensor orientations, while incapable of clearly depicting spatial information.

6.2 Interaction

To make full use of combined three-dimensional and projective display of a scattered moment tensor field, we provide both views with a list of interaction capabilities:

- *Highlighting*: When pointing at an eigenvector position in the stereographic view, both corresponding eigenvector directions are highlighted and connected to the sphere origin by line drawing while rendering a double-couple watermark in the background of the stereonet. The corresponding glyph in the three-dimensional view is highlighted by color and size change to allow matching of stereonet and glyph display.
- *Selection*: Users are able to use mouse based multiple tensor selection in both views to select, highlight or hide tensors. Affected glyphs and eigenvectors are highlighted, or hidden in both views.
- *Parameter Selection*: We provide the user with means to select a distance function for clustering, adjust ϵ_e, ϵ_d and change glyph type display as well as coloring (earthquake magnitude, CLVD fraction, etc.).
- *Similarity Querying*: Right click on a tensor M highlights all tensors N (glyphs and projected eigenvector directions) that satisfy $d(M, N) < \epsilon_e$ for the currently selected distance function and threshold.
- Clustering: Users can initiate clustering, toggle the display of individual cluster outlines, cluster members or representatives in both views.

All interaction methods aim to improve visual matching between the stereographic and the three-dimensional view of the data. Furthermore, they are designed to allow manual data exploration and analysis.

7. RESULTS

In the following, we present visualizations of two data sets containing moment tensor data from earthquakes in Chile and Tonga. Figure 6 (b) gives an impression of beachball based moment tensor visualization together with a stereonet projection with fixed projection point and slab geometry display. The same figure shows a color based clustering visualization using polarity glyphs. Polarity glyphs allow easy identification of wave propagation directions and CLVD tensors, by conveying magnitudes and directions by tensor shapes. The alternative rendering of the stereonet as a list view, showing one stereonet for each cluster, allows uncluttered visualization of clusters in projective space. Watermarking using average double-couple improves perception of fault directions in stereonet display. In general, the stereonet display shows the distribution of positive and negative wave propagation directions which is further aided by polarity glyph display. Figure 7 shows the benefit of information reduction by clustering. Clusters may be visualized by average tensors, outlines, cluster members or a combination of these. Cluster representatives are highlighted by color and size to be distinguishable from regular cluster members. The selected distance function (DC rotation) shows clear and correct clustering in projective and three-dimensional space. Cluster outlines show information about spatial location and size of frequent earthquake sources and avoid occlusion of individual earthquake sources.

Similarity querying as shown in Figure 8 is useful for quick identification of similar earthquake sources. Compared to clustering, it does not restrict its solution to local regions, but highlights tensors in all regions of the data set. While display of all clustering data such as outlines, and cluster members, as seen in Figure 8, may lead to a cluttered view if no manual selection is performed, it can be used to gain a quick overview of the structure of a moment tensor data set. For cluster outlining in stereographic space, the minimum spanning tree is not created in three-dimensional euclidean space, but corresponds to a minimum spanning tree on the surface of the sphere, connecting eigenvector directions along geodesic lines of the sphere. This tree commonly leads to two cluster outlines per cluster, separating major and minor eigenvector directions, as seen in Figures 7 and 8. Figure 9 (c) shows a selection of visualization settings for a small moment tensor cluster including outline visualization. The depicted average tensor is scaled to be distinguishable from regular cluster member and can be seen to be a well-aligned representative glyph. Correct cluster outlining is performed for arbitrary viewing angles. In contrast to the other presented results, which show the Chile data set, Figure 9 (a) compares the standard beachball visualization technique applied to the Tonga data set with our approach, yielding a far less cluttered view of the fault data. Figures 9 (b) shows visual feedback during orientation highlighting. In the presented data sets, clustering of moment tensors as well as geometry construction took less than a second on a PC with standard hardware (Intel Core 2 Duo @ 2 Ghz) and does not limit interactivity for small or medium sized data sets. For bigger data sets with a large number of tensors, QT clustering methods need additional optimizations, which are outside of the scope of this work.
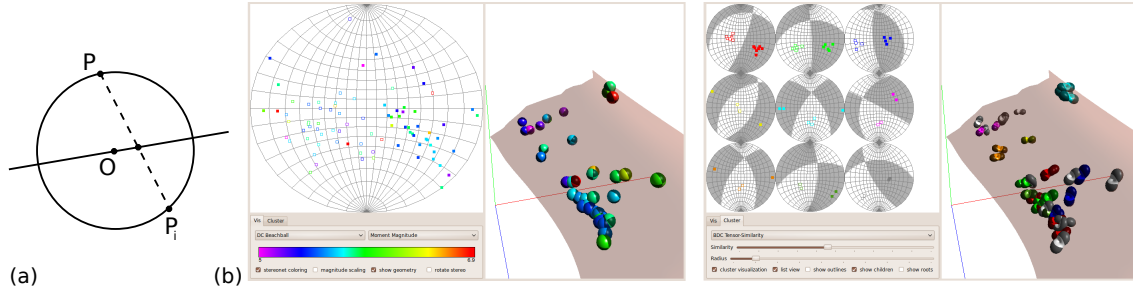
Figure 6. (a) Stereographic mapping procedure. (b) Left: Fixed-point stereonet projection shows longitudinal and equatorial lines along with major and minor eigenvector directions of tensors. Beachballs are colored by moment magnitude. Right: Cluster based polarity glyph coloring. Stereonet cluster-list shows average double-couple orientation as watermarks.
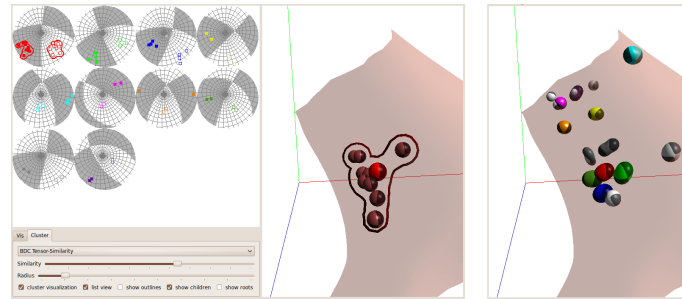

Figure 7. View dependent stereonet along with cluster selection and outlining in $\mathbb{R}^3$ and stereonet view. The representative glyph is displayed along with cluster members (left). Replacing cluster members by their respective cluster averages leads to a simplified and decluttered view of the tensor field and shows locations of frequent and similar seismic activities (right).

8. CONCLUSION AND FUTURE WORK

In this work we have introduced visualization techniques that aid the visual analysis of scattered moment tensors. We combine novel glyph based techniques with stereonet based projective renderings. A new clustering technique operating in moment and euclidean space allows the efficient reduction of redundant information, leading to less cluttered and more structured visualizations. This can be used as guide to identify similar earthquake mechanisms or sources. Various interaction techniques allow the direct mapping of information from projective to three-dimensional space. All presented methods lead to a higher information density than existing techniques and improve over the state of the art by conveying data properties that were previously hidden or hard to distinguish. Direction of future work includes the incorporation of further user preferences into the clustering process as well as enhanced display of additional geological information such as mantle geometry.
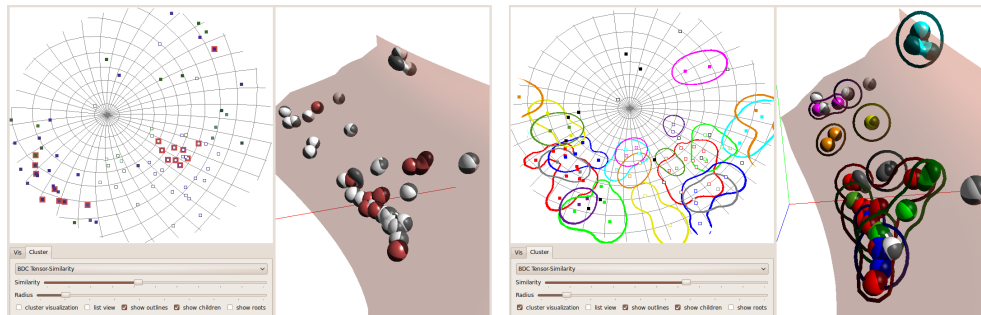

Figure 8. After user selection, tensors similar to a selected moment tensor are highlighted (left). Visualization of all identified clusters by outlining in projective and three-dimensional space (right).
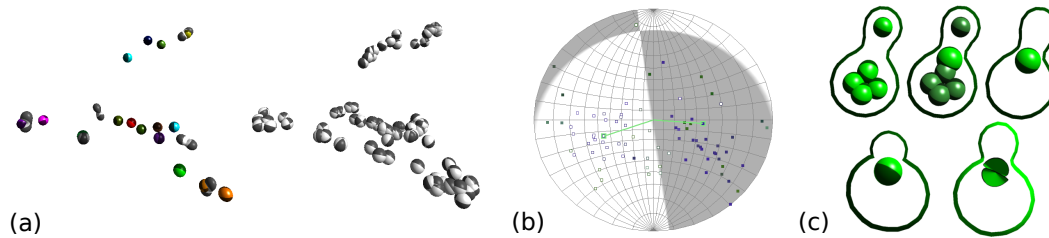
Figure 9. (a) Comparison of polarity glyph cluster averaging with unclustered beachball visualization. (b) Moment tensor highlighting in stereonet view shows related wave propagation directions and watermark. (c) Display of cluster members or the representative glyph can be toggled by the user. Correct outlining is preserved if changing the viewing angle. Display of slip geometry in a cluster allows a clearer look at geometrical segmentation in the form of fault planes and displacement discontinuities. Furthermore, the conic shape supports analysis of wave propagation directions and angles.

REFERENCES

[1] Özarslan, E. and Mareci, T. H., "Generalized diffusion tensor imaging and analytical relationships between diffusion tensor imaging and high angular resolution diffusion imaging," *MRM* **50**, 955–965 (2003).

[2] Weickert, J. and Hagen, H., [*Visualization and processing of tensor fields*], Springer Berlin (2006).

[3] Kindlmann, G. L., "Superquadric tensor glyphs," in [*VisSym*], Deussen, O., Hansen, C. D., Keim, D. A., and Saupe, D., eds., 147–154, Eurographics Association (2004).

[4] Moore, J., Schorn, S., and Moore, J., "Methods of classical mechanics applied to turbulence stresses in a tip leakage vortex," *J. of Turbomachinery* **118**(4), 622–629 (1996).

[5] Delmarcelle, T. and Hesselink, L., "Visualization of second-order tensor fields and matrix data," in [*IEEE Visualization*], Kaufman, A. E. and Nielson, G. M., eds., 316–323, IEEE Computer Society (1992).

[6] Ohtsu, M. and Shigeishi, M., "Theory and application of moment tensor analysis in AE," *Proc. of the Internat. Conf. on Emerging Technologies in NDT* , 19–26 (2004).

[7] Neeman, A., Jeremic, B., and Pang, A., "Visualizing tensor fields in geomechanics," in [*IEEE Visualization*], 35–42, IEEE Computer Society (2005).

[8] Hlawitschka, M., Scheuermann, G., and Hamann, B., "Interactive glyph placement for tensor fields," in [*Proc. of Third Internat. Sym. on Visual Computing*], 331–340, Springer (2007).

[9] Rohlfing, T., Sullivan, E., and Pfefferbaum, A., "Divergence-based framework for diffusion tensor clustering, interpolation, and regularization," in [*Proc. of IPMI*], 507–518, Springer (2007).

[10] Willemann, R., "Cluster analysis of seismic moment tensor orientations," *Geophys. J. Internat.* **115**(3), 617–634 (1993).

[11] Aki, K. and Richards, P., [*Quantitative seismology: Theory and methods*], Freeman San Francisco (1980).

[12] Knopoff, L. and Randall, M., "The compensated linear-vector dipole: a possible mechanism for deep earthquakes," *J. of Geophys. Research* **75**(26), 4957–4963 (1970).

[13] Haller, G., "Lagrangian structures and the rate of strain in a partition of two-dimensional turbulence," *Phys. of Fluids* **13**, 3365–3385 (2001).

[14] Haller, G., "An objective definition of a vortex," *J. of Fluid Mech.* **525**, 1–26 (2005).

[15] Pasternak, O., Sochen, N., and Basser, P. J., "The effect of metric selection on the analysis of diffusion tensor MRI data," *NeuroImage* **49**(3), 2190–2204 (2010).

[16] Kagan, Y., "3-D rotation of double-couple earthquake sources," *Geophys. J. Internat.* **106**(3), 709–716 (1991).

[17] Berthold, K. and Horn, P., "Closed-form solution of absolute orientation using unit quaternions," *J. of the Optical Society of America* **4**(4), 629–642 (1987).

[18] Heyer, L., Kruglyak, S., and Yooseph, S., "Exploring expression data: identification and analysis of coexpressed genes," *Genome research* **9**(11), 1106–1115 (1999).

[19] Blinn, J., "A generalization of algebraic surface drawing," *ACM Trans. on Graph.* **1**(3), 235–256 (1982).

[20] Leclercq, A., Akkouche, S., and Galin, E., "Mixing triangle meshes and implicit surfaces in character animation," in [*Proc. of Eurographic Workshop on Computer animation and simulation*], 37–47 (2001).